International Journal of Nanomedicine

Dovepress
Taylor & Francis Group

Open Access Full Text Article

ORIGINAL RESEARCH

Gallic Acid-Modified Graphene Oxide Nanocomposites Based Photothermal-Chemotherapy Enhancing Melanoma Immunotherapy

Yifan Feng[1], Wei Jin[1], Zhuo Li[1], Guangyu Fan[1], Jixiang Zhao[1], Minyu Zhu[1], Siming Wang[2], Yinghua Zhang[3], Ying Li[1,4–6], Zhengqi Dong[1,4–6]

[1]State Key Laboratory for Quality Ensurance and Sustainable Use of Dao-Di Herbs, Institute of Medicinal Plant Development, Chinese Academy of Medical Sciences, Peking Union Medical College, Beijing, 100193, People's Republic of China; [2]Northeast Asian Institute of Traditional Chinese Medicine, Changchun University of Chinese Medicine, Changchun, Jilin, 130117, People's Republic of China; [3]Department of Traditional Chinese Medicine, Jilin Provincial Academy of Chinese Medicine, Changchun, 130012, People's Republic of China; [4]Key Laboratory of Bioactive Substances and Resources Utilization of Chinese Herbal Medicine, Ministry of Education, Chinese Academy of Medical Sciences, Peking Union Medical College, Beijing, 100193, People's Republic of China; [5]Drug Delivery Center, Beijing Key Laboratory of Innovative Drug Discovery of Traditional Chinese Medicine (Natural Medicine) and Translational Medicine, Beijing, 100193, People's Republic of China; [6]Department of traditional Chinese medicine, Beijing Key Laboratory of Neuro-Innovative Drug Research and Development of Traditional Chinese Medicine (Natural Medicines), Beijing, 100193, People's Republic of China

Correspondence: Ying Li; Zhengqi Dong, Email yli@implad.ac.cn; zqdong@implad.ac.cn

Objective: Conventional therapy for the treatment of melanoma often results in poor therapeutic efficacy, and long-term and systemic administration of cancer chemotherapy is accompanied by unpredictable side effects. Graphene oxide (GO)-based photothermal therapy (PTT) combined with chemotherapy has emerged as a rapid and immunogenic alternative, where near-infrared (NIR) irradiation triggers localized hyperthermia via tumor-targeting photothermal immunomodulatory nanomaterials. However, pristine GO nanosheets tend to aggregate under physiological conditions, compromising their photothermal performance. This study aims to develop a combinatorial regimen integrating GO-enhanced photothermal immunotherapy with chemotherapy for synergistic melanoma treatment.

Methods: We fabricated a novel photothermal nanomaterial through gallic acid(GA) modification of GO (GAGO), with comprehensive characterization including UV-Vis spectroscopy, FTIR, XRD, and TEM to verify successful synthesis. The photothermal conversion efficiency was systematically evaluated, along with an investigation of the combined therapeutic efficacy and underlying mechanisms of GAGO with paclitaxel for melanoma treatment.

Results: In this study, GAGO was developed as a novel photothermal nanomaterial with enhanced dispersibility, superior stability, and reduced biotoxicity, which significantly improved the photothermal conversion efficiency of pristine GO. The synergistic combination of GA-GO-mediated photothermal therapy and paclitaxel chemotherapy effectively activated immune cells and potentiated T cell-mediated antitumor immunity, ultimately achieving remarkable tumor growth suppression.

Conclusion: We construct a synergistic platform of photothermal therapy, immunotherapy and chemotherapy, which provides a promising strategy for effective melanoma treatment.

Keywords: graphene oxide, gallic acid, melanoma, photothermal therapy, immunochemotherapy

Introduction

Melanoma stands out as the most aggressive and life-threatening form among skin cancers. It is highly prone to recurrence and metastasis, and the mortality rate is as high as 70–90% once the disease develops into a metastatic state.[1] Moreover, patients do not pay enough attention to it, and most of the patients are already in the advanced stage when they are diagnosed. Currently, surgical excision is the main treatment for melanoma, but it also has the shortcomings of large skin defects, long recovery time and high recurrence rate. In addition, chemotherapy and radiotherapy, as one of the most classic anti-tumor treatments, usually

Received: 10 April 2025
Accepted: 23 October 2025
Published: 15 November 2025

Graphical Abstract

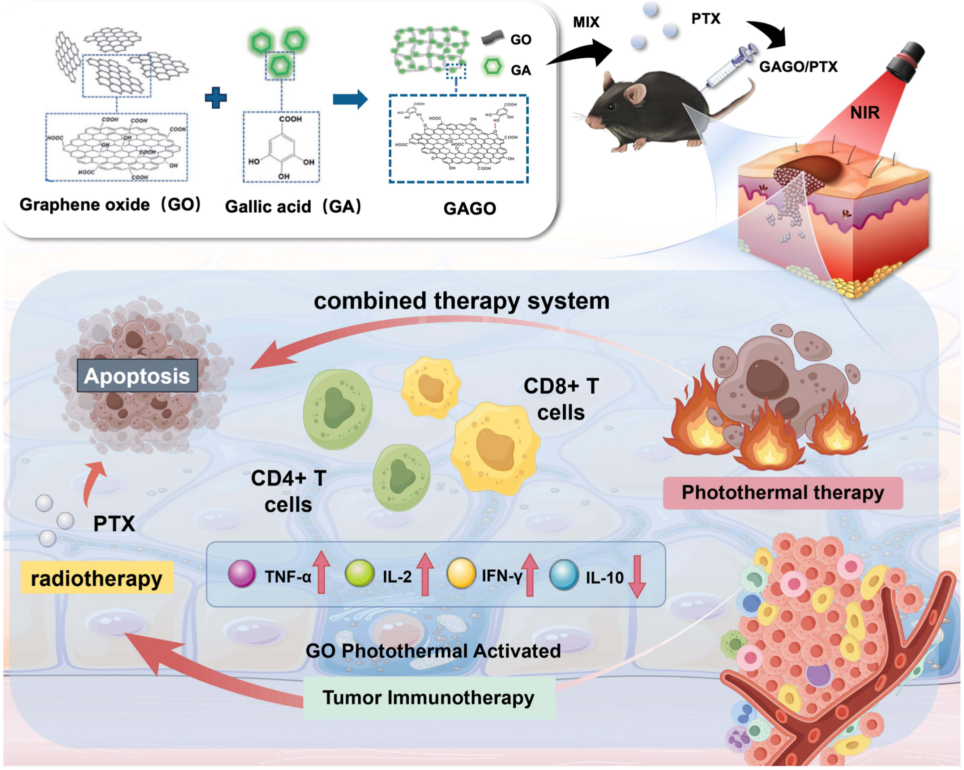

show unsatisfactory efficacy in melanoma treatment due to the poor response time and survival ability of patients, as well as the resistance of melanoma to chemotherapy drugs and the resistance to radiation. Paclitaxel (PTX), as an integral component of chemotherapeutic regimens for melanoma, exhibits a multifaceted toxicity profile in clinical practice. Its adverse effects manifest across multiple organ systems, including but not limited to myelosuppression, cumulative dose-dependent peripheral neuropathy, gastrointestinal disturbances, and hypersensitivity reactions. These toxicities necessitate comprehensive management strategies incorporating prophylactic premedication, dose optimization, and multidisciplinary supportive care to ensure therapeutic safety and efficacy.[2–4] Therefore, there is an urgent need to find safe and effective treatments for melanoma. Contemporary melanoma research has identified several innovative treatment modalities - including photothermal therapy (PTT), photodynamic therapy (PDT), gene therapy (GT), and immunotherapy (IT) - that demonstrate superior treatment outcomes, reduced systemic toxicity, and improved safety profiles compared to conventional approaches, suggesting significant clinical promise.

PTT enriches photothermal nanomaterials in tumor tissues and uses near-infrared radiation (NIR) to convert absorbed light into heat, resulting in local temperature increase, which will cause irreversible damage to cancer cells and directly allow selective ablation of tumor lesions.[5,6] NIR light-triggered PTT usually requires high temperatures >50°C to effectively ablate tumors, which may induce inflammation and heating damage to nearby normal organs.[7] In addition, it is challenging to deal with heat conduction and distribution within the tumor region during thermotherapy, which poses a significant obstacle to delivering a uniform thermal effect to the deeper tumor layers.[8] The potential risks posed to patients by photothermal nanomaterial toxicity, photothermal conversion efficiency, and laser power density for thermal therapy cannot be ignored. Therefore, current research primarily focuses on developing nanomaterials with improved dispersibility, low cytotoxicity, efficient in vivo clearance, excellent biocompatibility, and high photothermal conversion efficiency,[9,10] or incorporating nitric oxide (NO) to enhance PTT.[11] The synergistic strategy of combining PTT with chemotherapy ingeniously utilizes the localized hyperthermia generated by photothermal agents under near-infrared laser irradiation. This process not only directly ablates tumor cells but also enhances blood perfusion and vascular permeability within the tumor microenvironment. Li et al[12] developed a polymeric antitumor nanobomb (GEM806@PETU(CO)) for synergistic low-temperature photothermal/chemotherapy/gas therapy (LTPTT/CT/GT). This nanosystem features spatiotemporally controlled activation and synergistic therapeutic efficacy. Gao et al[13] constructed ARGN nanoclusters composed of gold nanorods (AuNRs) and rolling circle amplification products (RCA-p). This system achieves NIR irradiation-promoted release of siRNA-Plk1 and initiates combined photothermal/chemotherapeutic effects.

Graphene has emerged as a material of significant scientific interest owing to its exceptional combination of mechanical robustness, efficient photothermal conversion, remarkable flexibility, and superior heat transfer capabilities.[14] Graphene oxide (GO), as a graphene derivative, retains the special physicochemical properties such as photothermal performance while having lower dose-dependent toxicity and higher biocompatibility, and has a wide range of applications in the fields of catalysis, energy technology, composites, sensors, and nanoelectronics.[15–17] GO derivatives (GO/rGO) show exceptional immunostimulatory potential, engaging both immediate and antigen-specific immune pathways.[18] In studies by Orecchioni et al, administration of graphene, GO, and rGO via intravenous, intraperitoneal, intramuscular, and subcutaneous routes was shown to trigger rapid interactions with circulating and tissue-resident immune cells, resulting in immediate immune activation.[19] It has also been found that graphene-based materials can trigger immune regulation by binding to Toll-like receptors (TLRs), secreting a variety of Th 1/Th 2-related cytokines, such as granulocyte-macrophage colony-stimulating factor (GMCSF), tumor necrosis factor (TNF)-α, interleukin (IL)-10, IL-1α and IL-6 together with chemokines which include RANTES, MIP-1α, MIP-1β and MCP-1, and this immunomodulation can be enhanced by functionalized structural modifications.[20,21] Based on the abundant surface activity of GO, a large number of studies have focused on the use of GO as a delivery system for chemotherapeutic drugs, gene drugs, or immunostimulants. However, the immunostimulatory potential of GO-based nanomaterials remains underexplored, with only preliminary experimental evidence available to date.

Moreover, pristine GO nanosheets are prone to aggregate and form clusters in physiological state (high concentration of salts, proteins) therefore do not have the ability to become drug carriers, and GO contains a large amount of -OH, -COOH, C-O-C, which increases the distance between the layers, weakens the van der Waals forces between the layers, and destroys the hexagonal carbon stabilization of graphene, so that it is easier to be heat decomposition, and has poor thermal stability.[22–24]

To achieve the effect of reducing the dose while enhancing the photothermal conversion performance, natural polyphenolic components are a potential choice. Gallic acid (GA) exhibits excellent photothermal conversion capabilities that can be imparted to nanomaterials. Its molecular structure, containing multiple phenolic hydroxyl and carboxyl moieties, enables strong interfacial interactions with graphene oxide (GO) through hydrogen bonding and π-π stacking with oxygenated surface groups,[25,26] based on the coordination chemistry strategy. It can also further enhance the photothermal properties due to the intermolecular charge transfer effect,[27] which improves the dispersion of GO and the photothermal conversion efficiency. Zeng et al used GA-assisted modification to make glass (BG), changing its color from white to black, endowing it with a high light-barrier property and significantly enhancing its absorption of near-infrared light.[28] Hou et al developed a GA-assisted coordination strategy to synthesize a black calcium-based material, which was integrated with sequential photothermal therapy for synergistic treatment of bone tumors and defects, establishing a high-temperature tumor ablation approach.[29] In addition, polyphenol groups can bind to cancer cell surface receptors and also have some anti-tumor effects, making them a good natural material for modifying structural defects on GO surfaces.[30]

GA is a hydroxyphenolic compound with antimicrobial, anti-inflammatory and antitumor activities. We used it to functionalize GO through a simple surface modification strategy. The resulting GA-modified GO (GA-GO) nanocomposite demonstrates enhanced photothermal conversion efficiency and prolonged aqueous stability. High photothermal conversion performance was achieved at low doses, and the antitumor activity and immune activation ability of the GAGO nanomaterials combined with chemotherapy agent-paclitaxel was explored, which provides a basis for the development of a combined cancer inhibition approach based on GO for chemotherapy, phototherapy and immunotherapy.

Experimental Methods

Materials

GAGO was purchased from J&K Scientific (Beijing, China); GA was purchased from Sigma-Aldrich (Shanghai, China); paclitaxel injection (albumin type) (PTX), Cell-Counting-Kit-8 (CCK8), 4’,6-diamidino-2- phenylindole (DAPI) were purchased from Beyotime Biotechnology (Shanghai, China); fetal bovine serum (FBS), penicillin/streptomycin solution (PenStrep), and trypsin were purchased from Gibico (USA); B16 cell line was provided by pricella (Wuhan, China); Annexin V-FITC/ PI double staining kit was provided by Solarbio (Beijing, China); CD4 immunofluorescent antibody was purchased from Abcam (Shanghai, China); CD28 immunofluorescent antibody was purchased from CST (Beijing, China); TNF-α, IL-2, IFN-γ and IL-10 Elisa kits were provided by Invitrogen (USA).

Preparation of GAGO

GO powder of 25mg was weighed and dissolved in water under ice bath using ultrasonic probe for 1h, pH 4.75 was adjusted and gallic acid powder of 125mg was weighed and added to GO solution and allowed to fully dissolve. Magnetic stirring was done for 24h to enable full reaction. Removal of excess GA was achieved using a 1000 Da dialysis membrane over 48 hours, after which the GAGO solution was preserved at 4°C.

Characterization of GAGO

DLS measurements (n=3) of 0.8 mL nanosolution aliquots yielded average particle size, PDI, and zeta potential values. Carbon-supported 300-mesh copper grids were employed as substrates for GO/GAGO deposition in TEM sample preparation. After adsorption for 0.5 min, the excess solution was sucked from the edge portion with filter paper and left to stand for 20 min. The samples were then further dried in vacuum for 12 h. Electron microscope images were taken with a transmission electron microscope at an accelerating voltage of 200 KV. UV-vis spectra of GO, GA, and GAGO solutions were recorded from 200–800 nm using a standard quartz cuvette in a spectrophotometer, both GO and GAGO were prepared at identical concentrations of 1 mg/mL. A standard calibration curve was established by correlating absorbance at 262 nm with GA concentrations (0–0.01 mg/mL), yielding the linear equation $y = 0.0277x - 0.0005$ ($R^2 = 0.9997$). This curve subsequently enabled determination of drug loading (DL) and loading efficiency (LE) through quantitative GA analysis. Fourier infrared spectroscopy was used to analyze the nature of the surface functional groups of GO, GA, and GAGO using KBr pressed sheets in the wave number range of 400–4000 cm^{-1}. X-ray diffractograms of GO, GA, and GAGO were recorded by x-ray diffractometer for analysis. The working voltage and working current were set to 40 KV and 40 mA, and the start and end angles were 5° and 60°, respectively. Raman spectra were analyzed by 532 nm diode laser excitation to observe the structural differences between the samples.

$$\mathrm{DL} = \frac{\text{Weight of GA in GAGO}}{\text{Weight of GAGO}} \times 100\%$$

$$LE = \frac{\text{Weight of GA in GAGO}}{\text{Original GA added weight}} \times 100\%$$

Stability of GAGO

To investigate the stability of GAGO, GO, GAGO solutions were left at room temperature for 7 days and the change in particle size was measured every other day. The stability of GO and GAGO (1 mg/mL) was evaluated in various physiological environments—deionized water, phosphate-buffered saline (PBS, pH 7.4), and RPMI 1640 with 10% FBS—with subsequent measurements of hydrodynamic diameter and surface charge.

The Evaluation of Photothermal Performance

In vitro Evaluation of Photothermal Performance

The photothermal performance of the microneedles was evaluated using the near infrared (NIR) light irradiation method. The experiment was conducted by directly irradiating GO and GAGO solutions with an 808 nm infrared laser (MDL-III-808, China) using a 0.2 cm^2 spot area at power densities of 1.5 W/cm^2 and 2 W/cm^2 for 10 minutes. The stabilized temperature values were recorded, and real-time photothermal images were monitored using an infrared thermal imager (Guide T120, China). The photothermal stability of the microneedles was tested by turning the NIR laser on/off 3 times with the same parameter settings. The photothermal conversion efficiency is calculated by the following formula.

$$\eta = \frac{\mathrm{h}s\Delta T_{material} - \Delta T_{water}}{\mathrm{I} \times \left(1 - 10^{-A}\right)}$$

Where I represents laser power, A denotes the absorbance of the aqueous suspension at 808 nm, $\Delta T_{material}$ and ΔT_{water} indicate the temperature changes of the test sample and blank control (water) respectively. The heat transfer coefficient is expressed as h, while s represents the surface area of the container.[31]

In vivo Evaluation of Photothermal Performance

Female c57 mice of 6–8 weeks of age and weighing 18–22g were selected and acclimatized with standard food at 25°C for one week. For culture expansion of B16 melanoma cells, 100 μL of logarithmic growth phase B16 cell suspension (3×10^6 cells/mL) was collected, sterilized and inoculated subcutaneously on the back of c57 mice. When the tumor grew to 50–90mm^3 (7d), the in situ melanoma mouse model was successfully established.

The mice were divided into control, model, GO, GAGO, and GAGO/PTX groups, with the control group receiving no treatment while the other groups were established as melanoma models. The therapeutic agents were administered via intratumoral injection, after which all treatment groups underwent NIR irradiation at a power density of 1.5 W/cm^2 based on in vitro photothermal conversion results. Tumor temperature changes were monitored and recorded at 0, 1, 3, and 5 min during irradiation using an infrared thermal camera to evaluate the photothermal therapeutic effects.

Antitumor Ability in vitro

Cell Culture

B16 cells were maintained in RPMI 1640 medium, while HK-2 cells were cultured in DMEM/F12, both supplemented with 10% FBS (Gibico) and 1% penicillin-streptomycin (Gibico). All cells were incubated at 37°C under 5% CO_2.

Determination of Drug Concentration

B16 cells in logarithmic growth phase were plated in 96-well plates (1.0×10^4 cells/well). Following 24 h culture, the medium was refreshed with PTX-containing medium at graded concentrations (0.5–15 nM).[32] A blank control group was also included, with five replicate wells for each concentration. After an additional 24-hour culture, the medium was refreshed, and CCK-8 solution (10 μL/well) was introduced. Following 2–4 hours of incubation, optical density was measured at 450 nm with a microplate reader.

Cytotoxicity Experiment

10 nM PTX was added to a 1 mg/mL GAGO solution to prepare the GAGO/PTX suspension. Cell viability was assessed using a CCK-8 assay with OD450 measurements. B16 cells (5×10^3/well) were plated in 96-well plates and treated with varying concentrations of GAGO or GAGO/PTX combinations for 24 h. Photothermal effects were induced by 808 nm laser irradiation (2 W/cm^2, 5 min) to evaluate cytotoxicity in both B16 and HK-2 cell lines.

Detection of Apoptosis by Flow Cytometry

Plates were spread using six-well plates with a cell count of 2×10^5 cells/well, with an addition volume of 2.5 mL, and incubated overnight. Adding the blank medium diluted drug, respectively: blank group, PTX, GAGO, GAGO NIR, GAGO/PTX, GAGO/PTX NIR, and set up 3 duplicate wells in each group. After 24h of incubation with drug administration, the GAGO NIR group and GAGO/PTX NIR group were irradiated using an infrared laser (1.5 W/cm^2) for 5 min per well. Flow cytometry analysis of Annexin V-FITC and PI staining enabled quantification of early- and late-stage apoptotic cells. Fluorescence intensity was detected using flow cytometry.

Antitumor Ability in vivo

Mice Tumor Model Construction

Female c57 mice of 6–8 weeks of age and weighing 18–22 g were selected and acclimatized with standard food at 25°C for one week. For culture expansion of B16 melanoma cells, 100 μL of logarithmic growth phase B16 cell suspension (3×10^6 cells/mL) was collected, sterilized and inoculated subcutaneously on the back of c57 mice. When the tumor grew to 50–90 mm^3 (7d), the in situ melanoma mouse model was successfully established. The model mice were randomly divided into 7 groups, which were model group, NIR, PTX, GAGO, GAGO NIR(GN), GAGO/PTX(GP), and GAGO/PTX NIR(GPN). Another blank control group was set up, with a normal diet and saline administration, with 5 mice in each group.

Tumor Growth Curve and Tumor Suppression Rate Determination

All procedures were conducted at 25±2°C and 50±5% RH. Tumor-bearing mice received in situ injections on days 0 and 7, with select groups undergoing NIR irradiation (808 nm, 1.5 W/cm^2, 5 min). Tumor dimensions (a=longest diameter; b=perpendicular width) were measured every 48 h using calipers, with volumes calculated as $V=½ab^2$. On day 14, 24 h post-final treatment, mice were euthanized for serum collection (orbital bleeding) and organ harvest (heart, liver, spleen, lungs, kidneys, tumors). Excised tumors were photographed and measured before tissue processing (24 h fixation, paraffin embedding, sectioning) for H&E, TUNEL, and Ki67 staining. Tumor-infiltrating T cells were analyzed by immunofluorescence using CD3/CD4/CD8 antibodies. The protein expression profiles of HSP70 and HSP90 were analyzed using Western blotting. The serum levels of alanine aminotransferase (ALT), aspartate aminotransferase (AST), blood urea nitrogen (BUN), and creatinine (CRE) were measured in the collected blood samples.

Statistical Analysis

All results are expressed as mean ± standard deviation. GraphPad Prism software was utilized for statistical analysis, applying Student's t-tests (two groups) or one-way ANOVA (≥3 groups) to calculate p-values. The statistical differences were considered at $*p < 0.05$, $**p < 0.01$, $***p < 0.001$, $****p < 0.0001$, not significant (n.s). $p > 0.05$.

Result and Discussion

Synthesis and Characterization of GAGO Nanocomposites

GA is a natural polyphenol widely distributed in plants and fruits. Studies have shown that it is positively charged under acid and negatively charged under alkaline conditions.[33] Although GO is theoretically amphiphilic, in practice, graphene sheets tend to agglomerate with each other due to intermolecular hydrogen bonding interactions. GO carries a negative surface charge, when the pH is adjusted to a weakly acidic environment, the electrostatic interaction between GA and GO can promote self-assembly. Therefore, we propose to modify it with GA to prepare GO nanocomposites that can be stably dispersed in aqueous solutions and physiological media for a long time.[34]

The preparation of synthesized GAGO was immediately examined for particle size, polydispersity index (PDI) and zeta potential. The particle size of the GAGO was about 227.73±23.22 nm, the PDI was 0.15 ± 0.02, and the Zeta potential was about −40.33±1.52 mV. Zeta potential serves as a critical indicator of nanoparticle stability, where higher absolute values correlate with stronger interparticle electrostatic repulsion, thereby enhancing colloidal stability. The zeta potential of GO was measured to be −33 ± 3.6 mV, showing a significant difference compared to that of GAGO (Figure 1A).

The morphological and structural features of as-synthesized GAGO were characterized by transmission electron microscopy (TEM) (Figure 1B). While GO exhibits characteristic wrinkled film morphology consistent with literature reports, GA functionalization yields a markedly flatter GAGO structure. This morphological transition confirms successful GA loading through observable structural modifications.

The absorption spectra (Figure 1C) of GA, GO and GAGO were measured in the range of 200–800 nm using a UV-Vis spectrophotometer to determine the peak absorbance. GO has a strong absorption peak at 235 nm due to the π→π jump of the C=C ring bond. GA exhibits two similar peaks at 212 and 262 nm. While the characteristic peak of GAGO moved to 221 nm. The results indicated that the loading of GA in GO was successful and formed GAGO nanocomposites.

The FTIR spectra of GO, GA, and GAGO are shown in Figure 1D. It can be observed that the peaks of GO at 3406.34, 1857.11, 1623.95 and 1101.14 cm^{-1} are associated with OH, C=O, C=C and C-O stretching modes, respectively. GA's

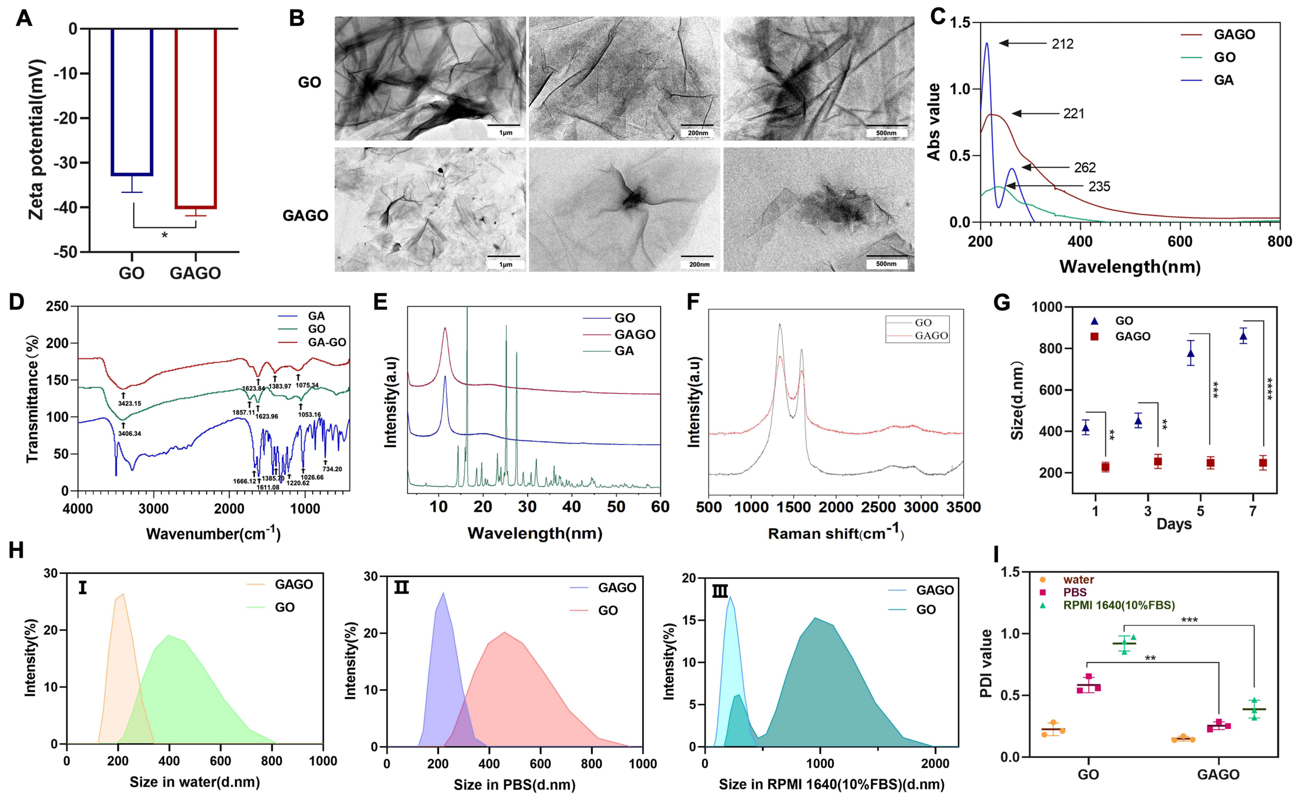

Figure 1 GAGO nanomaterials characterization. (**A**) Comparison of zeta potentials of GO and GAGO. (**B**) TEM image of GA and GAGO. (**C**) UV-Vis absorbance spectra of GA, GO, and GAGO samples. (**D**) FTIR spectra of GA, GO, and GAGO. (**E**) XRD patterns of GA, GO, and GAGO measured at 40 kV and 40 mA with a scanning rate of 5°/min and 2ϴ angles ranging from 5° to 60°. (**F**) Raman spectra of GO and GAGO obtained using 532 nm diode laser excitation. (**G**) Changes in particle size of GO and GAGO left in aqueous solution for 7 days. (**H**) Comparison of particle size of GO and GAGO in water (I), PBS (II), RPMI 1640 (10% FBS) (III). (**I**) Comparison of PDI between GO and GAGO in water, PBS, RPMI 1640 (10% FBS). The error bars indicate means ± SD and n =3. Significance was assessed by using *t*-test; *$p < 0.05$, **$p < 0.01$, ***$p < 0.001$, ****$p < 0.0001$.

molecular structure was confirmed through characteristic FTIR peaks: 1666.12 cm^{-1} (phenolic O-H), 1611.08 cm^{-1} (aromatic C=C), 1220.62 cm^{-1} (carboxyl C=O), 1026.66 cm^{-1} (carboxyl C-O), and 734.20 cm^{-1} (benzene ring δCC). The IR spectra of GA-loaded graphene oxide (GAGO) showed characteristic signals of GO and GA, indicating successful loading.

The structures of GO, GA, and GAGO nanocomposites were evaluated using XRD analysis (Figure 1E). The XRD spectra of GA showed several characteristic peaks at 16.5°, 25.4°, and 27.65° at 2ϴ degree, representing the highly crystalline structure of GA. The XRD pattern of GO displayed a characteristic diffraction peak at 2θ = 11.40°, attributed to interlayer oxygen-containing functional groups (eg, carboxyl, hydroxyl, and epoxy groups). In contrast, GAGO nanocomposites showed amorphous characteristics.

Defects and disorder in the GO and GAGO structures were investigated using Raman spectroscopy (Figure 1F). The D band is 1334 cm^{-1} and the G band is 1594 cm^{-1} for GO and GAGO. The D band indicates the disorder of the sp2 carbon network. While pristine GO shows sharp D-peaks, GAGO exhibit broadened D-bands due to disrupted sp^2 networks from oxidation-induced damage.

Stability Study of GAGO

From the results of 7-day continuous monitoring of the particle size, PDI, and zeta potential of GAGO, it can be observed that GAGO nanoparticles can remain stable at room temperature for several days. Over the course of 7 days, the particle size of GAGO remained stable within the range of 227.73–248.33 nm (Figure 1), and the PDI was maintained between 0.184 and 0.251. In contrast, the particle size of GO increased from 419.33 ± 35.8 nm to 861.33 ± 37.42 nm, and the PDI increased from 0.332 to 0.934. Overall, GAGO exhibited good stability at room temperature and could be stored for an extended period.

https://doi.org/10.2147/IJN.S531001

Further investigation into the changes in particle size and PDI of GO and GAGO in different media (Figure 1) revealed that in water, the particle size of GO was 400.93 ± 15.93 nm, and the PDI was 0.225 ± 0.05. In PBS, the particle size slightly increased to 487.07 ± 15.6 nm, and the PDI increased to 0.584 ± 0.06. In RPMI 1640 (10% FBS), the changes were more significant, with the particle size of GO increasing to 1068.67 ± 115.79 nm and the PDI reaching 0.92 ± 0.06. In contrast, the particle size of GAGO showed minimal changes, remaining stable at around 200 nm, with the PDI maintained between 0.15± 0.02 and 0.39± 0.07. GAGO demonstrated stability in all three media, which is attributed to the π-π interactions between the aromatic rings of GA and the sp^2 carbon regions of GO, enhancing the stability of the composite material.

Evaluation of GAGO Photothermal Conversion Performance

The photothermal conversion efficiency of GAGO was characterized under 808 nm NIR laser irradiation at two power densities (1.5 and 2 W/cm^2). Both GO and GAGO aqueous dispersions were exposed for 10 minutes while an infrared thermal imaging system continuously monitored temperature changes and captured thermal distribution profiles. The schematic diagram of the experiment is provided in Figure 2A. The infrared thermal maps (Figure 2C) revealed that both the concentration of GAGO and the power of the infrared light source significantly influenced the photothermal effect of the nano-solutions. Statistical analysis of the temperature data (Figure 2B) showed that under irradiation with a power density of 2 W/cm^2, the temperature of the 1000 μg/mL GAGO solution reached the highest value of 54.4 ± 1.41°C, while the temperature of the GO solution at the same power density and concentration was only 48.17 ± 2.70°C. As the concentration of GAGO decreased, the temperature also decreased accordingly. As shown in Figure 2D, at a fixed GAGO concentration, the solution temperature progressively increased with higher irradiation power, demonstrating its photothermal tunability. The temperature changes of GO and GAGO solutions irradiated at 2 W/cm^2 were recorded every minute over a 10min (Figure 2E). It was observed that the 1000 μg/mL GAGO solution exhibited the fastest heating rate and stabilized within 100 seconds, confirming its photothermal tunability. After the temperature stabilized, the light source was turned off, and the process was repeated three times consecutively. The temperature remained around 48°C, demonstrating its photothermal stability (Figure 2F). The photothermal conversion efficiency (η) of GAGO was calculated to be 56.5 ± 1.3% under 2 W/cm^2 irradiation at a concentration of 1000 μg/mL. The in vivo photothermal conversion capability of GAGO/PTX was evaluated using infrared thermography to record local tumor temperature. As shown in Figure 2G, the saline-injected blank and Model groups slightly increased their temperatures under laser irradiation. In contrast, the local temperature of GAGO/PTX tumors increased dramatically. Its temperature reached 48°C in 5 min, indicating that GAGO/PTX has an excellent in vivo photothermal effect, and can kill tumors by thermal ablation (Figure 2H).

It can be seen that the introduction of GA enhances the photothermal conversion performance of GAGO. GA provides a more stable photothermal conversion environment for the composites and reduces the energy loss through the intermolecular hydrogen bonding and π-π interactions of the GO lamellae tightly connected. It has also been found that it may promote the transfer of photogenerated electrons and reduce the complexation of electron-hole pairs, thus improving the photothermal conversion efficiency.[35,36]

In vitro Antitumor Activity of GAGO

IC_{50} is an index used to evaluate the in vitro antitumor effect. In order to investigate the optimal PTX concentration for the combination of GAGO and PTX, the cytotoxicity of PTX was firstly detected at 0.5 nM–15 nM using CCK8 method. The results showed that the cell survival rate was 51% at a concentration of 10nM, so the PTX concentration of 10 nM was selected for the in vitro antitumor assay of the combination (Figure 3A). The in vitro antitumor activity of GAGO photothermal therapy combined with PTX was further evaluated, and it was found that the addition of GAGO could increase the tumor cell inhibitory rate of the single chemotherapeutic agent at the same concentration of PTX in the B16 cell line. And the effect of PTX combined with GAGO photothermal therapy was significantly stronger than that of PTX alone (Figure 3B).

This was detected by flow cytometry, in which a significant difference in cell viability was observed between the GAGO/PTX NIR and Control groups (Figure 3C). In the GAGO NIR group, the introduction of NIR enhanced the cytotoxicity of GAGO alone, leading to the death of a few B16 cells. This further confirms the effectiveness of PTX combined with GAGO photothermal therapy for melanoma.

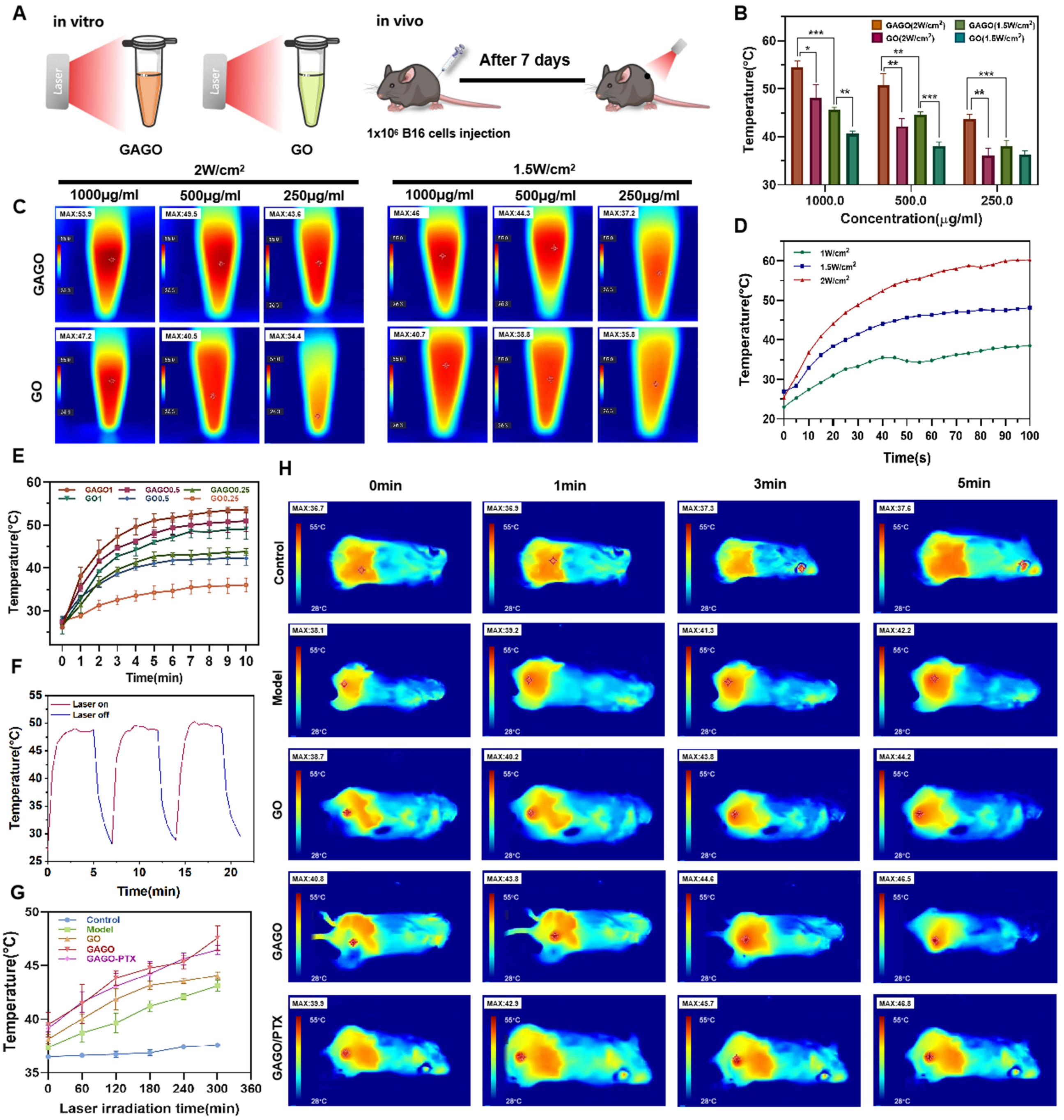

Figure 2 The photothermal conversion performance of GO and GAGO. (**A**) Schematic illustration of in vivo and in vitro photothermal conversion experiments. (**B**) The temperature of GO and GAGO solutions after 10 minutes of infrared light irradiation. (**C**) Infrared thermal imaging maps of GO and GAGO under infrared light irradiation at power densities of 1.5 W/cm^2 and 2 W/cm^2. (**D**) Temperature changes of GAGO solution under 1, 1.5, and 2 W/cm^2 NIR irradiation. (**E**) The temperature variations of GO and GAGO solutions at different concentrations under infrared light irradiation at varying power densities over a 10min. (**F**) The temperature changes of the GAGO solution in response to turning the infrared laser on and off. (**G**) Temperature changes at the tumor site in mice within 5 min of infrared irradiation. (**H**) In vivo infrared thermal imaging of photothermal conversion in mice. The error bars indicate means ± SD and n =3. Significance was assessed by using *t*-test; *$p < 0.05$, **$p < 0.01$, ***$p < 0.001$.

Antitumor Effect in vivo

In vivo anti-melanoma studies were performed on B16 hormonal mice according to the indicated protocols (Figure 4A). Tumor growth volume and tumor weight were measured in mice that were injected intratumorally with saline only, with the PTX-administered group as a positive control. The efficacy of several therapeutic strategies, including GAGO

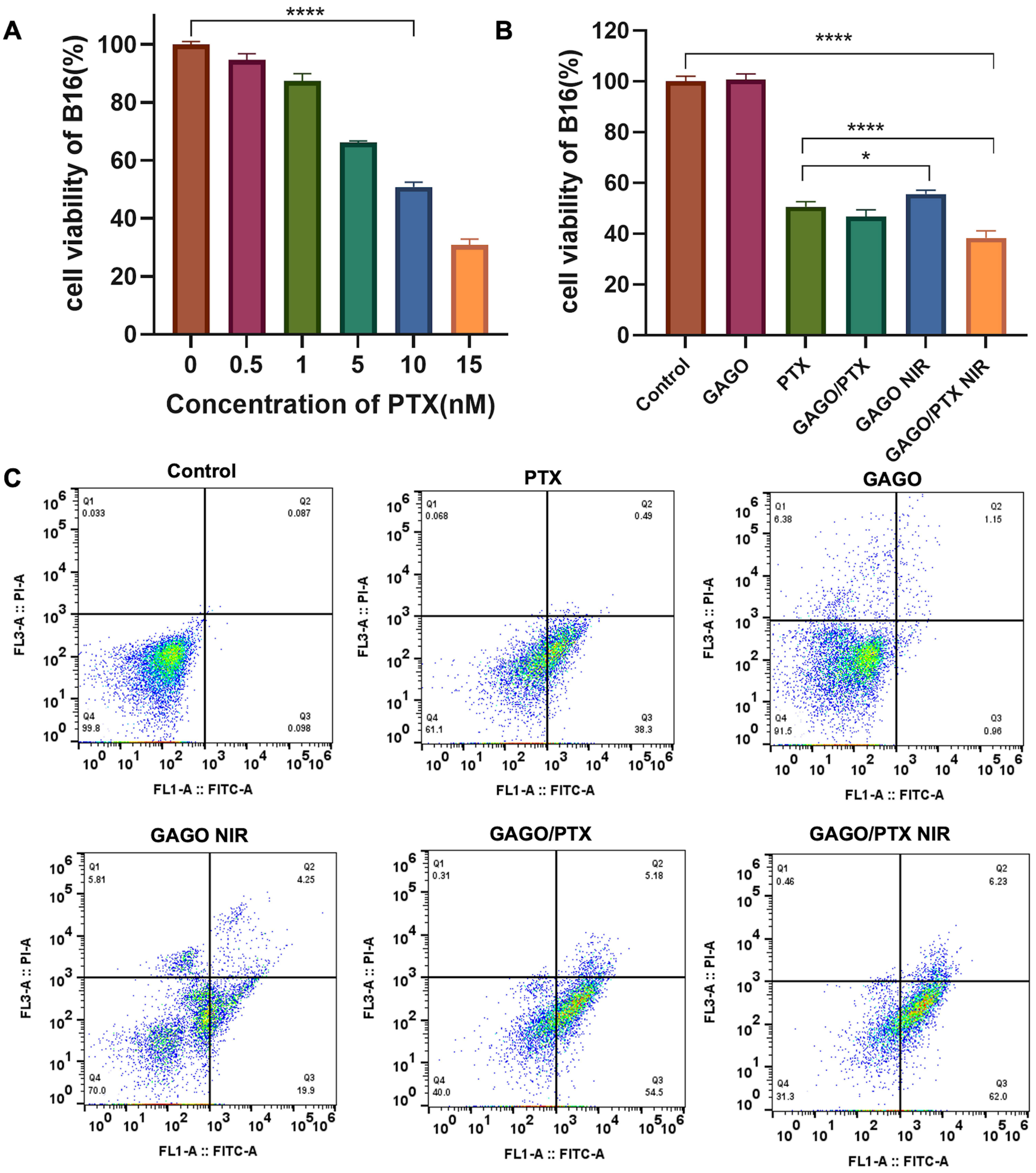

Figure 3 The in vitro inhibitory effects of GAGO on the B16 cell line. (**A**) Exploration of the IC50 concentration of PTX. (**B**) Cytotoxicity of GAGO, GAGO/PTX, GAGO NIR and GAGP/PTX NIR under different treatment regimens. (**C**) The apoptosis induced by different treatment regimens of GAGO, GAGO/PTX, GAGO NIR, and GAGO/PTX NIR was detected using flow cytometry. The error bars indicate means ± SD and n =5. Significance was assessed by using *t*-test; *p < 0.05,****p < 0.0001.

photothermal therapy (GAGO NIR,GN), GAGO in combination with PTX therapy (GAGO/PTX, GP), and GAGO photothermal therapy in combination with PTX therapy (GAGO/PTX NIR,GPN), were evaluated in focus.

As shown in Figure 4B, all treatment groups showed some efficacy and no significant weight loss was observed in the mice. The use of GAGO alone had no significant inhibitory effect on tumors, consistent with the results of cellular experiments; the use

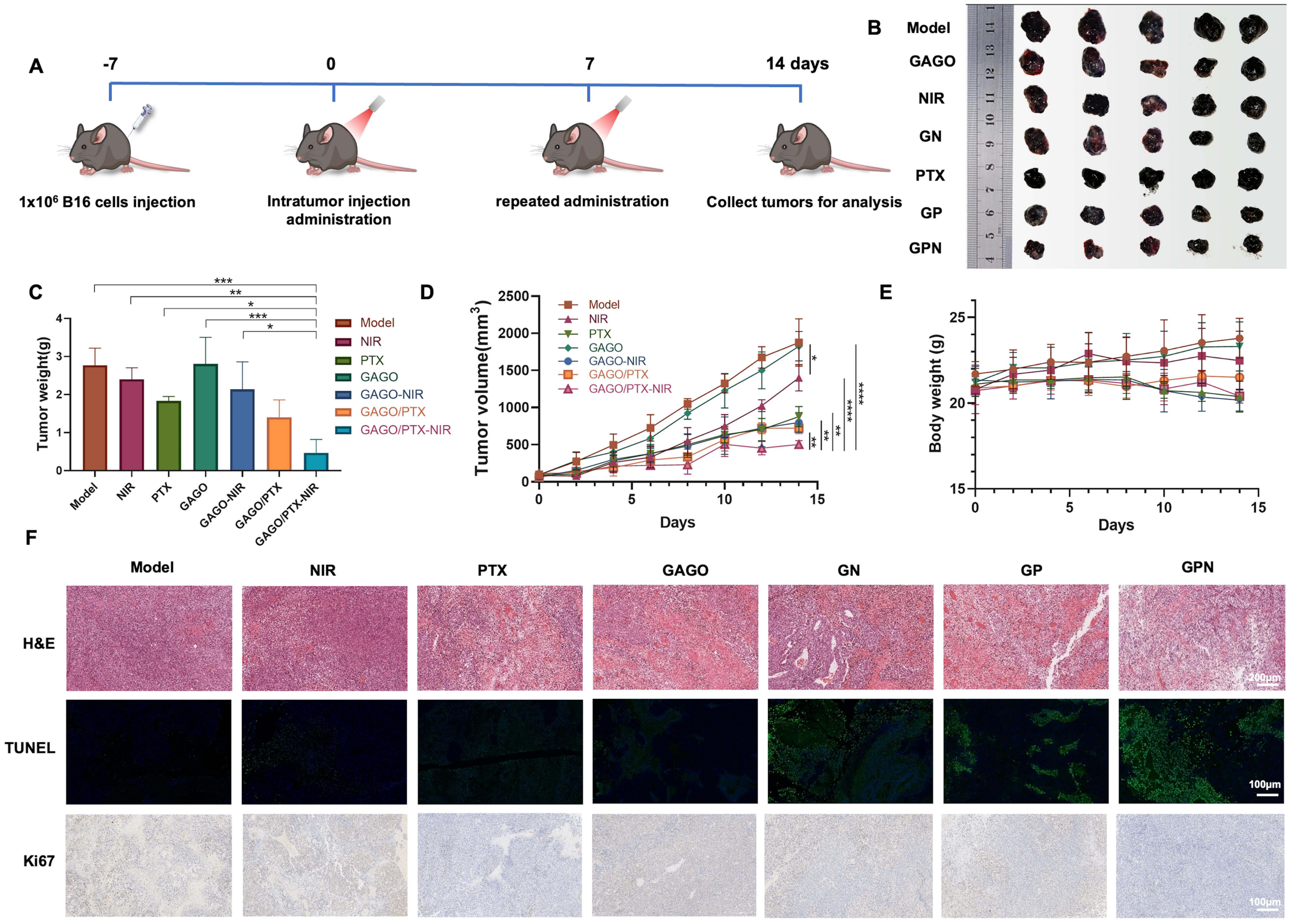

Figure 4 In vivo evaluation of photothermal conversion performance and antitumor pharmacodynamics in mice. (**A**) Tumor modeling in mice and the timeline of the treatment regimen. (**B**) Images of tumors in mice after different treatment regimens. (**C**) Tumor weights in different groups of mice. (**D**) Tumor volumes in mice. (**E**) Changes in body weight of mice during the treatment period. (**F**) H&E staining of tumor tissue sections, Scale bar: 200μm, TUNEL immunofluorescence staining of tumors, Scale bar: 100μm, and Ki67 immunohistochemical (IHC) staining, Scale bar: 100μm. The error bars indicate means ± SD and n =5. Significance was assessed by using the *t*-test; *p < 0.05, **p < 0.01, ***p < 0.001, ****p < 0.0001.

of NIR infrared laser irradiation alone had some therapeutic effect in the early stage of the treatment, but was not sufficient to completely inhibit tumor growth in the later stage of the treatment; GAGO/PTX NIR also showed superior tumor growth inhibition compared with the PTX-positive drug group; GAGO/PTX significantly inhibited tumor growth, but not significantly compared with the positive drug group; and GAGO/PTX significantly inhibited tumor growth, but not significantly compared with the positive drug group. However, there was no significant difference compared with the positive drug, and the efficacy of GAGO/PTX NIR group was more significant (Figure 4C–E).

In order to further verify the in vivo therapeutic effect, the tumors were collected for H&E, Ki67 and TUNEL staining at the end of treatment (Figure 4F). The H&E results showed that the stained sections of tumor tissues in the control group showed typical tumor pathological features, such as tightly arranged tumor cells and abundant blood vessels. In contrast, the GAGO NIR, GAGO/PTX and GAGO/PTX NIR of the treatment group showed a large number of necrotic and cell-free areas, among which, the signal of GAGO/PTX NIR staining of the periplasmic plasma was significantly weakened compared with that of the model group, resulting in larger necrotic areas and the appearance of a large number of white gaps, which indicated that the tumor's extracellular matrix (ECM) had been damaged and the tumor had been damaged and the tumor had been damaged. Matrix (ECM) was severely damaged.[37]

TUNEL staining, a technique used to detect apoptosis, identifies apoptotic cells by labeling the 3'-OH end of DNA breaks, the nuclei of positive cells showed green fluorescence indicating the presence of DNA breaks suggesting apoptosis, and the nuclei of negative cells showed blue color using DAPI staining. The results showed that the fluorescence signals of GAGO

NIR, GAGO/PTX, and GAGO/PTX NIR were stronger compared to other groups, indicating that GAGO/PTX NIR triggered significant apoptosis.

Ki67 is a nuclear protein associated with cell proliferation and is commonly used to assess the proliferative activity of tumor cells. In immunohistochemistry (IHC), the expression level of Ki67 is reflected by staining intensity.[38] A positive coloration of the nucleus in brown color indicates that it is in the proliferative cycle. Statistical analysis revealed all treatment groups differed significantly from the model control ($p<0.05$). However, only the GAGO/PTX NIR combination demonstrated marked differences versus PTX alone ($p<0.01$), confirming its superior anti-proliferative efficacy.

Mechanism of Tumor Immune Activation

Immunofluorescence staining was performed to assess T cell infiltration within the tumor tissue. As illustrated in Figure 5A and B, negligible T cell infiltration was observed in the Model group, with weak fluorescence signals detected in both the NIR and GAGO groups. In contrast, significant infiltration of CD4+ T cells and CD8+ T cells was evident in the tumor tissues of the PTX, GP, GN, and GPN groups. The relative fluorescence intensities of CD3+CD4+ and CD3+CD8+ T cells were quantified for each treatment group relative to the Model group. While the Model and NIR groups exhibited similar responses, neither demonstrated statistically meaningful variation from baseline ($p>0.05$). However, the CD3+CD4+ fluorescence signal in the GPN group was markedly enhanced compared to the Model group, though it did not differ significantly from the PTX group. Fluorescence microscopy demonstrated intense CD3+CD8+ dual-positive staining exclusively in GPN-treated specimens, with other groups showing only baseline signals. This enhanced T cell infiltration is likely attributable to the photothermal effect, which increases local blood flow and disrupts the tumor barrier, thereby facilitating the recruitment and penetration of T cells into the tumor microenvironment.[39]

To further investigate cytokine levels in tumor tissues, we quantified IL-2, TNF-α, IFN-γ, and IL-10 concentrations using ELISA kits (Figure 5C–F). Compared to the Model group, the NIR group exhibited no significant differences in TNF-α, IL-2, or IFN-γ levels. All treatment groups except GAGO showed significantly elevated TNF-α and IL-2 levels, while IFN-γ levels were significantly increased across all treatment groups. Notably, the GN and GPN groups demonstrated markedly higher IFN-γ levels compared to the PTX group. Concurrently, all treatment groups displayed significantly reduced IL-10 levels relative to the Model group, with the GPN group showing greater IL-10 suppression than the PTX group. Mechanistically, TNF-α binds to tumor necrosis factor receptors (TNFRs) on tumor cells, activating the caspase cascade to induce apoptosis while simultaneously damaging tumor vascular endothelial cells.[40] IL-2 and IFN-γ synergistically promote CD8+ T cell proliferation, activation, and enhanced infiltration into the tumor microenvironment.[41] Conversely, the Th2-associated cytokine IL-10 suppresses IFN-γ synthesis, potentially explaining the observed CD8+ T cell hyperactivity in the GPN group. Collectively, these findings demonstrate that GPN therapy exerts critical immunomodulatory effects by enhancing immune cell proliferation, differentiation, and effector functions, ultimately reshaping the antitumor immune landscape.[42]

We further analyzed the expression of heat shock proteins HSP70 and Hsp90 in tumor tissues by Western blot and found that both HSP70 and HSP90 were upregulated in all treatment groups (Figure 5G). A growing body of research has demonstrated that heat shock proteins (HSPs) can stimulate innate immune responses.[43] Hyperthermia treatment induces tumor cells to activate their endogenous heat shock protein (HSP) genes, leading to increased HSP expression in the tumor microenvironment, which further promotes the proliferation of tumor-killing T cells and exerts anti-tumor effects.[44]

Sufficient thermal stimulation triggers HSP70 on tumor cells to activate NK cells, enhancing their production of inflammatory cytokines such as IL-2, IFN-γ, and TNF-α, thereby strengthening cell-mediated or humoral immune responses against tumors. Additionally, HSP90 can form complexes with tumor antigens (eg, mutated proteins), which are taken up by dendritic cells (DCs) via the CD91 receptor. Such enhancement of antigen processing and cross-presentation via MHC class I pathways elicits robust CD8+ T cell responses, forming the scientific basis for Hsp90-derived cancer vaccines.[45]

As pivotal regulators of the adaptive immune system, CD4+ T cells execute multiple functions: directing Th cell specialization, amplifying CD8+ T cell effector populations, and supporting antibody generation by B lymphocytes.[46,47] Conversely, aberrant differentiation of CD4+ Th cells into dysfunctional subsets may lead to the secretion of immunomodulatory cytokines such as IL-10, IL-17, and IFN-γ, which exert pleiotropic effects on immune regulation.[48,49] Notably, a subset of Th cells expresses granzymes and perforin, enabling direct cytolytic activity against tumor cells

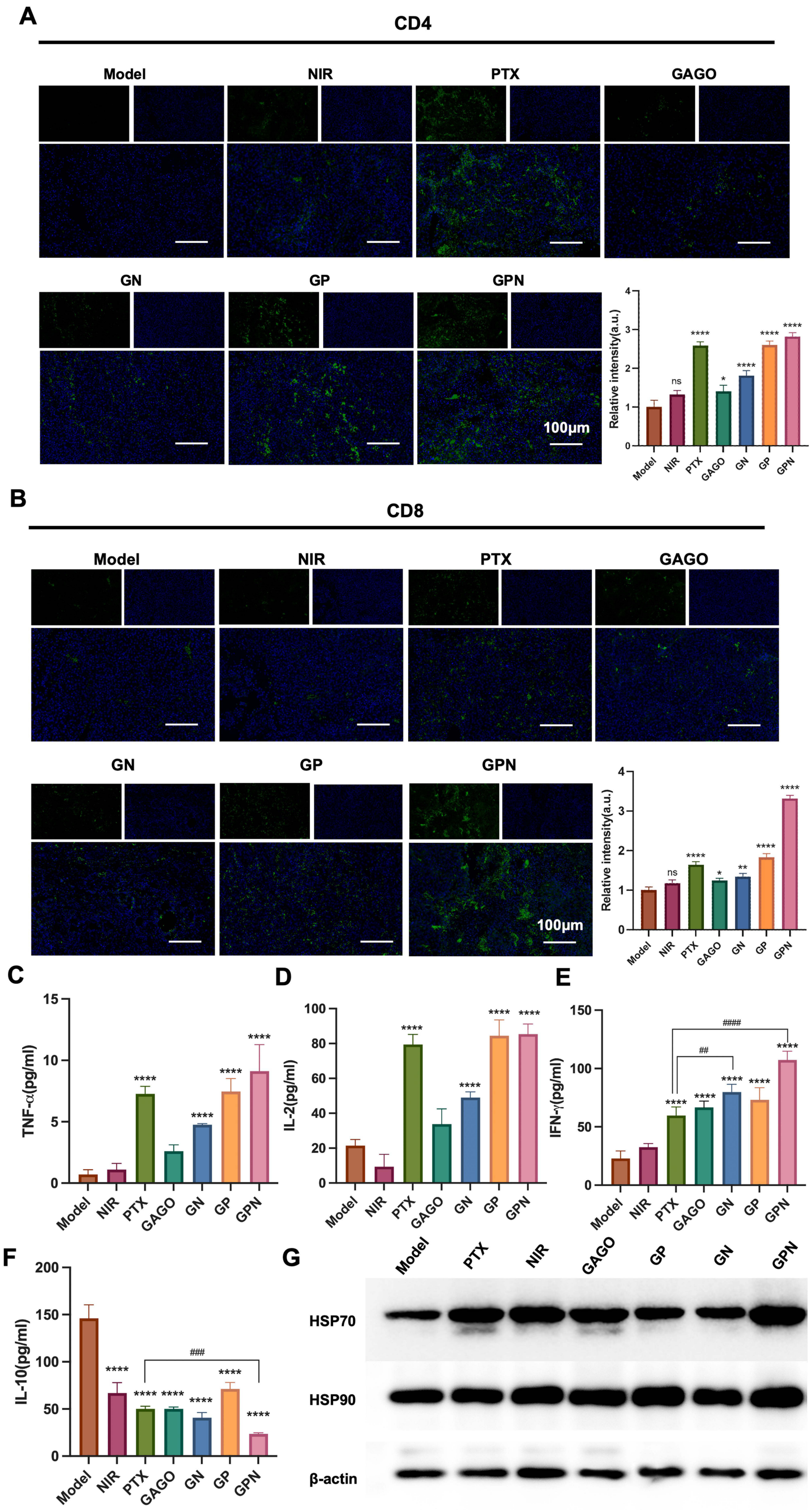

Figure 5 Mechanism of in vivo antitumor action. (**A**) Fluorescence images of CD4+ T cells in tumor tissues (The scale bar is 100 μm) (**B**) Fluorescence images of CD8+ T cells in tumor tissues (The scale bar is 100 μm) (**C**–**F**) Levels of TNF-α, IL-2, IL-6, IL-10 in different groups. Scale bar: 100μm. (**G**) Results of Western blot analysis of HSP70 and HSP90. The error bars indicate means ± SD and n =5. Significance was assessed by using the *t*-test; *p < 0.05, **p < 0.01, ****p < 0.0001. $^{\#\#}$p < 0.01, $^{\#\#\#}$p < 0.001, $^{\#\#\#\#}$p < 0.0001.

https://doi.org/10.2147/IJN.S531001

presenting antigens via MHC class II molecules.[50] These mechanisms collectively contribute to tumor cell elimination, remodeling of the tumor microenvironment (TME), and establishment of immunological memory.[51] CD8+ T cells, or cytotoxic T lymphocytes (CTLs), recognize MHC class I-presented antigenic peptides through T cell receptors (TCRs), thereby executing targeted tumor cell lysis.[52–54]

The crosstalk between CD4+ and CD8+ T cells is integral to the cancer-immunity cycle.[55,56] Church et al demonstrated that tumor-specific CD4+ T cells critically sustain the functional capacity of tumor-infiltrating CD8+ T cells.[57] Their findings revealed reduced PD-1 expression on CD8+ T cells in the presence of CD4+ T cells, suggesting that CD4+ T cells attenuate CD8+ T cell exhaustion. Mechanistically, tumor-specific CD4+ T cells enhance CD8+ T cell recruitment, clonal expansion, and effector differentiation through IFN-γ-dependent chemokine signaling and IL-2 production.[58] Furthermore, CD4+ T cell-mediated help preferentially augments the functionality of high-affinity TCR-expressing CD8+ T cells while fostering TME conditions conducive to the infiltration of low-affinity CD8+ T cell clones.[59]

Safety Evaluation of GAGO

HK-2 cells are a cell line isolated and immortalized from normal human renal proximal tubular epithelial cells. It retains many properties of renal tubular epithelial cells and is widely used in renal physiology, pathology and toxicology studies. In order to test whether GAGO is cytotoxic, HK-2 and B16 cell lines were co-cultured with different concentrations of GAGO in vitro for 24 hours and then subjected to CCK8 assay for cell viability (Figure 6A). The results showed that the cell growth was similar to that of the control group, which indicated that GAGO does not exhibit significant cytotoxicity in the absence of NIR near-infrared light excitation. Mouse heart, lung and spleen tissues were further observed by tissue staining to assess the toxicity of photothermal therapy in concert with chemotherapy (Figure 6B). The results showed that the GPN group did not induce structural changes in the heart, lung and spleen of mice. Biochemical analysis of serum samples revealed significant hepatorenal toxicity in the PTX group, as evidenced by markedly elevated levels of ALT, AST, BUN, and CRE (Figure 6C). Notably, these pathological alterations were substantially reversed through combination therapy. Therefore, GPN did not produce significant toxicity in vivo.

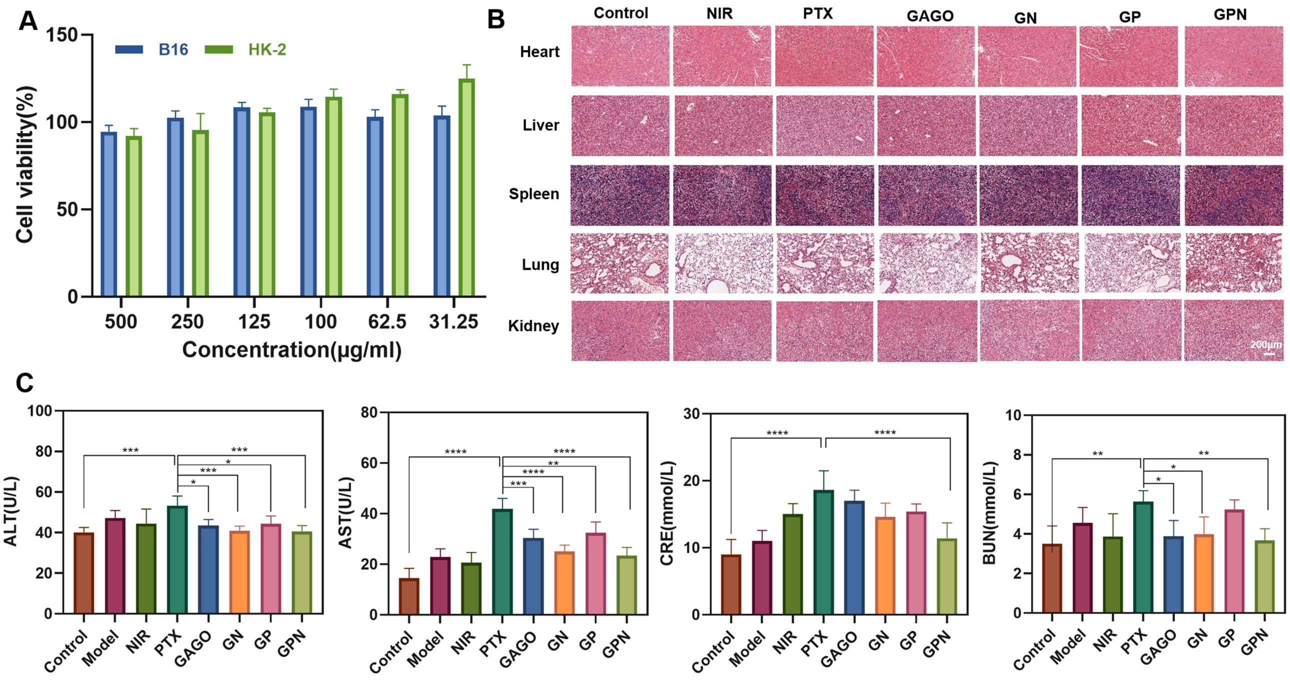

Figure 6 In vivo and in vitro safety evaluation of GAGO. (**A**) Cytotoxicity of GAGO in B16 and HK-2 cell lines. (**B**) H&E-stained tissue sections of the heart, liver, spleen, lung, and kidney from each group. Scale bar: 200μm. The error bars indicate means ± SD and n =5. (**C**) serum levels of ALT, AST, CRE, and BUN. Significance was assessed by using the *t*-test; *p < 0.05, **p < 0.01, ***p < 0.001, ****p < 0.0001.

Conclusion

In summary, we successfully constructed a novel photothermal nanocomposite-GAGO with high stability, high photothermal conversion efficiency and high biosafety for the synergistic treatment of tumors with the chemotherapeutic drug PTX. The successful synthesis was verified by UV, FTIR, XRD and RAMAN spectroscopy. The good photothermal properties and biocompatibility of GAGO were evaluated by in vitro experiments. For in vivo experiments, the GAGO/PTX NIR showed excellent anti-tumor effects, which attributed to the chemotherapy and enhanced immune responses by effectively activating CD4+ T and CD8+ T cells proliferation, and promoting the secretion of TNF-αand IFN-γ. This synergistic therapeutic regimen had significant tumor inhibitory effects, which confirms a promising and effective therapeutic pathway for melanoma.

Ethical Approval

The study was conducted in accordance with the US National Institutes of Publication, 8th Edition, 2011), and approved the Laboratory Animal Ethics Committee of the Institute of Medicinal Plant Development, Peking Union Medical College (protocol code: SLXD-20241119016 and date of approval: 12 November 2024).

Funding

This work was financially supported by the National Natural Science Foundation of China (No. 82304733), CAMS Innovation Fund for Medical Science (CIFMS) (No. 2022-I2M-1-018, No. 2022-I2M-2-001, No. 2021-I2M-1-022), Jilin Scientific and Technological Development Program (No. 20230401102YY and No. 2025020409YY). The project is supported by Key project at central government level. “The ability establishment of sustainable use for valuable Chinese medicine resources” (2060302).

Disclosure

The authors report no conflicts of interest in this work.

References

1. Gui J, Guo Z, Wu D. Clinical features, molecular pathology, and immune microenvironmental characteristics of acral melanoma. *J Transl Med*. 2022;20(1):367. doi:10.1186/s12967-022-03532-2
2. Dülgar Ö, Saha A, Elleson KM, et al. Successful treatment with carboplatin and paclitaxel in melanoma progression after immune-related adverse events. *Immunotherapy*. 2023;15(13):993–999. doi:10.2217/imt-2022-0213
3. Di Pietro FR, Marinelli D, Verkhovskaia S, et al. Weekly carboplatin plus paclitaxel chemotherapy in advanced melanoma patients resistant to anti-PD-1 inhibitors: a retrospective, monocentric experience. *BMC Cancer*. 2024;24(1):1220. doi:10.1186/s12885-024-12961-9
4. Gebhardt C, Simon SCS, Weber R, et al. Potential therapeutic effect of low-dose paclitaxel in melanoma patients resistant to immune checkpoint blockade: a pilot study. *Cell Immunol*. 2021;360:104274. doi:10.1016/j.cellimm.2020.104274
5. Chen MC, Lin ZW, Ling MH. Near-infrared light-activatable microneedle system for treating superficial tumors by combination of chemotherapy and photothermal therapy. *ACS Nano*. 2016;10(1):93–101. doi:10.1021/acsnano.5b05043
6. Kadkhoda J, Tarighatnia A, Tohidkia MR, et al. Photothermal therapy-mediated autophagy in breast cancer treatment: progress and trends. *Life Sci*. 2022;298:120499. doi:10.1016/j.lfs.2022.120499
7. Du L, Wang P, Huang H, et al. Light-activatable and hyperthermia-sensitive “all-in-one” theranostics: NIR-II fluorescence imaging and chemo-photothermal therapy of subcutaneous glioblastoma by temperature-sensitive liposome-containing AIEgens and paclitaxel. *Front Bioeng Biotechnol*. 2023;11:1343694. doi:10.3389/fbioe.2023.1343694
8. Ren Y, Ma S, Zhang D, et al. Functionalized injectable hyaluronic acid hydrogel with antioxidative and photothermal antibacterial activity for infected wound healing. *Int J Biol Macromol*. 2022;210:218–232. doi:10.1016/j.ijbiomac.2022.05.024
9. Xiao F, Liu Y, Su Y, et al. Biodegradable Poly(amino acid)-Bismuth nanotheranostic agents for CT/MR imaging and photothermal-chemodynamic synergistic therapy. *Chem Bio Eng*. 2024;1(5):448–460. doi:10.1021/cbe.4c00078
10. Liang S, Liu Y, Zhu H, et al. Emerging nitric oxide gas-assisted cancer photothermal treatment. *Exploration*. 2024;4(6):20230163. doi:10.1002/EXP.20230163
11. He J, Song R, Xiao F, et al. Cu(3)P/1-MT nanocomposites potentiated photothermal-immunotherapy. *Int J Nanomed*. 2023;18:3021–3033. doi:10.2147/IJN.S414117
12. Li Z, Li T, Chen S, et al. Friends fight the foes: synergistic low-temperature photothermal/chemo/gas therapy for conquering cancer cells. *Adv Funct Mater*;2025. e14605. doi:10.1002/adfm.202514605
13. Gao Q, Wang W, Sun S, et al. Bundling gold nanorods with RCA-produced DNA tape into an intelligently reconfigurable nanocluster bomb for multimodal precision cancer therapy. *Mater Today Bio*. 2025;32:101718. doi:10.1016/j.mtbio.2025.101718
14. Lu J, Zhang A, Zhang F, et al. Ganoderenic acid D-loaded functionalized graphene oxide-based carrier for active targeting therapy of cervical carcinoma. *Biomed Pharmacother*. 2023;164:114947. doi:10.1016/j.biopha.2023.114947

15. Cui G, Wu J, Lin J, et al. Graphene-based nanomaterials for breast cancer treatment: promising therapeutic strategies. *J Nanobiotechnol*. 2021;19 (1):211. doi:10.1186/s12951-021-00902-8
16. Shamsi S, Abdul Ghafor AAH, Norjoshukrudin NH, et al. Stability, toxicity, and antibacterial potential of Gallic Acid-Loaded Graphene Oxide (GAGO) against Methicillin-Resistant Staphylococcus aureus (MRSA) Strains. *Int J Nanomed*. 2022;17:5781–5807. doi:10.2147/IJN.S369373
17. Singh G, Nenavathu BP, Imtiyaz K, Moshahid ARM. Fabrication of chlorambucil loaded graphene- oxide nanocarrier and its application for improved antitumor activity. *Biomed Pharmacother*. 2020;129:110443. doi:10.1016/j.biopha.2020.110443
18. Yunus MA, Ramli MM, Osman NH, Mohamed R. Stimulation of innate and adaptive immune cells with graphene oxide and reduced graphene oxide affect cancer progression. *Arch Immunol Ther Exp*. 2021;69(1):20. doi:10.1007/s00005-021-00625-6
19. Orecchioni M, Bedognetti D, Sgarrella F, Marincola FM, Bianco A, Delogu LG. Impact of carbon nanotubes and graphene on immune cells. *J Transl Med*. 2014;12(1):138. doi:10.1186/1479-5876-12-138
20. Saleem J, Wang L, Chen C. Immunological effects of graphene family nanomaterials. *NanoImpact*. 2017;5:109–118. doi:10.1016/j.impact.2017.01.005
21. Zhou H, Zhao K, Li W, et al. The interactions between pristine graphene and macrophages and the production of cytokines/chemokines via TLR- and NF-κB-related signaling pathways. *Biomaterials*. 2012;33(29):6933–6942. doi:10.1016/j.biomaterials.2012.06.064
22. Yeh CN, Raidongia K, Shao J, Yang QH, Huang J. On the origin of the stability of graphene oxide membranes in water. *Nat Chem*. 2014;7 (2):166–170. doi:10.1038/nchem.2145
23. Kaur K, Jindal R, Meenu. Self-assembled GO incorporated CMC and Chitosan-based nanocomposites in the removal of cationic dyes. *Carbohydr Polym*. 2019;225:115245. doi:10.1016/j.carbpol.2019.115245
24. Yang Y, Ma W, Li Z, Zhang Z, Hu Z. Graphene non-covalently functionalized with Gallic acid (Ga) as high performance electrode material for supercapacitors. *J Sci*. 2022;7(1):100386.
25. Cao L, Li Z, Su K, Cheng B. Hydrophilic graphene preparation from gallic acid modified graphene oxide in magnesium self-propagating high temperature synthesis process. *Sci Rep*. 2016;6:35184. doi:10.1038/srep35184
26. Li Y, Chen M, Yan J, et al. Tannic acid/Sr(2+)-coated silk/graphene oxide-based meniscus scaffold with anti-inflammatory and anti-ROS functions for cartilage protection and delaying osteoarthritis. *Acta Biomater*. 2021;126:119–131. doi:10.1016/j.actbio.2021.02.046
27. Xu J, Younis MR, Zhang Z, et al. Mild heat-assisted polydopamine/alginate hydrogel containing low-dose nanoselenium for facilitating infected wound healing. *ACS Appl Mater Interfaces*. 2023;15(6):7841–7854. doi:10.1021/acsami.2c21516
28. Zeng H, Ying Z-R, Luo X, et al. Gallic acid-modified bioglass with combined photothermal and antibacterial effects for the regeneration of infected diabetic wound. *Composites Part B*. 2023;257:110668. doi:10.1016/j.compositesb.2023.110668
29. Hou X, Zhang L, Chen Y, et al. Photothermal switch by gallic acid-calcium grafts synthesized by coordination chemistry for sequential treatment of bone tumor and regeneration. *Biomaterials*. 2025;312:122724. doi:10.1016/j.biomaterials.2024.122724
30. Dorniani D, Saifullah B, Barahuie F, et al. Graphene oxide-gallic acid nanodelivery system for cancer therapy. *Nanoscale Res Lett*. 2016;11(1):491. doi:10.1186/s11671-016-1712-2
31. Xi D, Xiao M, Cao J, et al. NIR light-driving barrier-free group rotation in nanoparticles with an 88.3% photothermal conversion efficiency for photothermal therapy. *Adv Mater*. 2020;32(11):e1907855. doi:10.1002/adma.201907855
32. Kundranda MN, Niu J. Albumin-bound paclitaxel in solid tumors: clinical development and future directions. *Drug Des Devel Ther*. 2015;9:3767–3777. doi:10.2147/DDDT.S88023
33. Martakov IS, Shevchenko OG, Torlopov MA, Gerasimov EY, Sitnikov PA. Formation of gallic acid layer on γ-AlOOH nanoparticles surface and their antioxidant and membrane-protective activity. *J Inorg Biochem*. 2019;199:110782. doi:10.1016/j.jinorgbio.2019.110782
34. Liu G, Yu R, Lan T, Liu Z, Zhang P, Liang R. Gallic acid-functionalized graphene hydrogel as adsorbent for removal of chromium (iii) and organic dye pollutants from tannery wastewater. *RSC Adv*. 2019;9(46):27060–27068. doi:10.1039/C9RA05664E
35. Ren S, Wang Q, Zhang C, Du R, Meng J, Zhang R. Layer-by-layer multitargeting strategy for enhanced photothermal therapy. *ACS Omega*. 2025;10(6):5460–5467. doi:10.1021/acsomega.4c07611
36. An L, Yan C, Mu X, et al. Paclitaxel-induced ultrasmall gallic acid-Fe@BSA self-assembly with enhanced MRI performance and tumor accumulation for cancer theranostics. *ACS Appl Mater Interfaces*. 2018;10(34):28483–28493. doi:10.1021/acsami.8b10625
37. Feng X, Zeng L, Wu L, et al. Self-delivery nanodrug to manipulate tumor microenvironment for boosting photodynamic cancer immunotherapy. *Biomed Pharmacother*. 2024;178:117220. doi:10.1016/j.biopha.2024.117220
38. Jiang Z, Xu H, Wang H, Sun J, Wang T, Sun M. Microneedles-mediated calcium-ion-modulated nanoamplifier for potentiating photodynamic therapy via specific-tuning assembly and tumor microenvironment remold. *Biomed Pharmacother*. 2024;177:117063. doi:10.1016/j.biopha.2024.117063
39. He T, Luo Y, Zhang Q, et al. Hyalase-mediated cascade degradation of a matrix barrier and immune cell penetration by a photothermal microneedle for efficient anticancer therapy. *ACS Appl Mater Interfaces*. 2021;13(23):26790–26799. doi:10.1021/acsami.1c06725
40. Marzagalli M, Ebelt ND, Manuel ER. Unraveling the crosstalk between melanoma and immune cells in the tumor microenvironment. *Semin Cancer Biol*. 2019;59:236–250. doi:10.1016/j.semcancer.2019.08.002
41. Ma H, Yang X, Ke J, et al. Smart assembled human serum albumin nanocarrier enhanced breast cancer treatment and antitumor immunity by chemo- photothermal therapy. *ACS Biomater Sci Eng*. 2020;6(5):3217–3229. doi:10.1021/acsbiomaterials.0c00286
42. Yang C, Lei J, Kang X, et al. A yeast cell wall derived hybrid hydrogel with photothermal and immune combined modality therapy for enhanced anti-melanoma efficacy. *Int J Nanomed*. 2023;18:5423–5440. doi:10.2147/IJN.S409674
43. Vostakolaei MA, Hatami-Baroogh L, Babaei G, Molavi O, Kordi S, Abdolalizadeh J. Hsp70 in cancer: a double agent in the battle between survival and death. *J Cell Physiol*. 2021;236(5):3420–3444. doi:10.1002/jcp.30132
44. Albakova Z, Mangasarova Y. The HSP immune network in cancer. *Front Immunol*. 2021;12:796493. doi:10.3389/fimmu.2021.796493
45. Eppink B, Krawczyk PM, Stap J, Kanaar R. Hyperthermia-induced DNA repair deficiency suggests novel therapeutic anti-cancer strategies. *Int J Hyperthermia*. 2012;28(6):509–517. doi:10.3109/02656736.2012.695427
46. Guo M, Liu MYR, Brooks DG. Regulation and impact of tumor-specific CD4(+) T cells in cancer and immunotherapy. *Trends Immunol*. 2024;45 (4):303–313. doi:10.1016/j.it.2024.02.005
47. Oh DY, Fong L. Cytotoxic CD4(+) T cells in cancer: Expanding the immune effector toolbox. *Immunity*. 2021;54(12):2701–2711. doi:10.1016/j.immuni.2021.11.015
48. Bawden EG, Wagner T, Schröder J, et al. CD4(+) T cell immunity against cutaneous melanoma encompasses multifaceted MHC II-dependent responses. *Sci Immunol*. 2024;9(91):eadi9517. doi:10.1126/sciimmunol.adi9517

49. Ye Y, Wang C, Zhang X, et al. A melanin-mediated cancer immunotherapy patch. *Sci Immunol*. 2017;2(17). doi:10.1126/sciimmunol.aan5692.
50. Shi C, Fu W, Zhang X, et al. Boosting the immunoactivity of T cells by resonant thermal radiation from electric graphene films for improved cancer immunotherapy. *Adv Ther*. 2023;6(2):2200163. doi:10.1002/adtp.202200163
51. Deng X, Guan W, Qing X, et al. Ultrafast low-temperature photothermal therapy activates autophagy and recovers immunity for efficient antitumor treatment. *ACS Appl Mater Interfaces*. 2020;12(4):4265–4275. doi:10.1021/acsami.9b19148
52. Espinosa-Carrasco G, Chiu E, Scrivo A, et al. Intratumoral immune triads are required for immunotherapy-mediated elimination of solid tumors. *Cancer Cell*. 2024;42(7):1202–1216.e1208. doi:10.1016/j.ccell.2024.05.025
53. Lee SJ, Lee HS, Hwang YH, et al. Enhanced anti-tumor immunotherapy by dissolving microneedle patch loaded ovalbumin. *PLoS One*. 2019;14 (8):e0220382. doi:10.1371/journal.pone.0220382
54. Marrella A, Giannoni P, Pulsoni I, Quarto R, Raiteri R, Scaglione S. Topographical features of graphene-oxide-functionalized substrates modulate cancer and healthy cell adhesion based on the cell tissue of origin. *ACS Appl Mater Interfaces*. 2018;10(49):41978–41985. doi:10.1021/acsami.8b15036
55. Chen DS, Mellman I. Oncology meets immunology: the cancer-immunity cycle. *Immunity*. 2013;39(1):1–10. doi:10.1016/j.immuni.2013.07.012
56. Preusser M, Berghoff AS, Thallinger C, Zielinski CC. Cancer immune cycle: a video introduction to the interaction between cancer and the immune system. *ESMO Open*. 2016;1(3):e000056. doi:10.1136/esmoopen-2016-000056
57. Church SE, Jensen SM, Antony PA, Restifo NP, Fox BA. Tumor-specific CD4+ T cells maintain effector and memory tumor-specific CD8+ T cells. *Eur J Immunol*. 2014;44(1):69–79. doi:10.1002/eji.201343718
58. Bos R, Sherman LA. CD4+ T-cell help in the tumor milieu is required for recruitment and cytolytic function of CD8+ T lymphocytes. *Cancer Res*. 2010;70(21):8368–8377. doi:10.1158/0008-5472.CAN-10-1322
59. Bos R, Marquardt KL, Cheung J, Sherman LA. Functional differences between low- and high-affinity CD8(+) T cells in the tumor environment. *Oncoimmunology*. 2012;1(8):1239–1247. doi:10.4161/onci.21285